ENCIT-2018
DESIGN AND ASSEMBLING OF A MAGNETIC CIRCUIT FOR A THERMOMAGNETIC MOTOR APPARATUS

Kaneko, G. H.[1]
Pg400422@uem.br
Trevizoli, P. V.[1,2]
paulo.trevizoli@gmail.com
Souza, A. C.[1]
acsouza@uem.br
Moro, F.[1,3]
f212043@dac.unicamp.br
Colman, F. C.[1]
fccolman@uem.br
Concerição, W. A. S.[1]
wasconceicao@gmail.com
Alves, C. S.[1]
csalves@uem.br

[1]Department of Mechanical Engineering. State University of Maringá. Av. Colombo, 5790 - Campus Universitario, 87020-900. Maringá/PR
[2]Department of Mechanical Engineering. Ingá University Center. Rod PR 317, 6114 – Parque industrial 200, 87035-510. Maringá/PR
[3]Department of Mechanical Engineering. State University of Campinas. R. Mendeleyev, 200 – Cidade Universitária, 13083-860. Campinas/SP

Abstract. *The operating principle of a thermomagnetic motor is due to the magnetic phase transition (ferro↔ paramagnetic) of magnetic materials around their transition, or Curie, temperature. The main components of a thermomagnetic motor are the magnetic material and the magnetic circuit. If the magnetic material presents the Curie temperature around the room temperature, it may have potential to be applied in thermomagnetic motors. Today are known several first and second order transition magnetic materials with Curie temperature of 20ºC and above. These materials also present large magnetocaloric effect. The magnetic circuit is responsible to guarantee a high magnetic field region which magnetically interacts with the magnetic material. This way, the main objective of the present research is to design a thermomagnetic motor to test different magnetic materials. However, we first introduce in this paper the design and assembly procedure of a magnetic circuit, currently under construction at State University of Maringá.*

Keywords: *Thermomagnetic motor, magnetic circuit, magnetization, magnetocaloric effect*

1. INTRODUCTION

The research and development of thermomagnetic motors is an open study field. The first descriptions of thermomagnetic motors date from late 1800's by the patents of Edison (1888) and Tesla (1889). More recently, with the discovery of novel magnetic materials with magnetic transition, or Curie, temperature around room temperature, the developments of thermomagnetic motors came back into attention (KARLE, 2001; CHRISTIAANSE AND BRÜCK, 2013; ALVES *et al*, 2014). These new materials present coupled magnetic and structural first order transition, with a large entropy change (or magnetocaloric effect, MCE) around the transition temperature (PECHARSKY *et al*, 2001; SMITH *et al*, 2012; GUTFLEISCH *et al*, 2016). As well magnetocaloric heat pumps (BARCLAY and STEYERT, 1982; TREVIZOLI *et al*, 2016), a large MCE is useful to increase the magnetic motor performance, and the abrupt change on the magnetic order, characteristic of first order transitions, is well suitable for applications in thermomagnetic motor. Therefore, first order magnetocaloric materials with large MCE have potential for such applications. Thermal hysteresis (GUTFLEISCH *et al*, 2016), however, may represent a significant limitation and reduce the applicability of some materials.

The operating principle of a thermomagnetic motor is due to the magnetic phase transition (ferro↔ paramagnetic) around the Curie temperature (T_{Curie}). The thermodynamic cycle is based on Ericson cycle, which is composed by two isothermal and two isofield curves. Fig. 1(a) presents a characteristic curve of Magnetization (M) versus Applied

Magnetic Field (B) of a magnetic material, while Fig. 1(b) a characteristic curve of Magnetization (M) versus Temperature (T). Fig. 1(c) shows the Temperature versus entropy (s), T-s diagram, of the Ericson cycle. Fig. 2 show a schematic diagram of the Ericson cycle.

Starting at point 1, where the magnetic material (MM) is ferromagnetic at a high field (T_{low} means below T_{Curie}), the material is then heated, by a hot stream, at constant B_{High} up to the point 2, changing the magnetic phase from ferro to paramagnetic (T_{low} to T_{high}). At point 2 - paramagnetic phase ($T_{high} > T_{Curie}$) - the magnetic material is not attacked by the magnetic field and can be easily moved ("work done on the system" by a spring in Fig. 2) from the high field to the low field region (B_{high} to $B_{low} \approx 0$). At point 3, the material is cooled, by a cold stream, at a constant B_{low} from T_{high} to T_{low}, returning to the ferromagnetic phase. At point 4 - ferromagnetic phase - the material is now attacked by the magnetic field, hence, moving from point 4 to point 1. Physically, the magnetic attraction of the process 4 to 1 produce movement and work ("work done by a shaft"). The area inside the M vs. B (or T-s) diagram is proportional to the work done by the cycle:

$$W = V \oint B \cdot dM(T, B) \qquad (1)$$

where V is the volume. The MCE, or isothermal entropy variation, is verified when the magnetic field is varied ($B_{high} \leftrightarrow B_{low}$): steps (2 to 3) and (4 to 1) in Fig. 1(c). As larger is the entropy variation, larger is the area and, consequently, the gross work:
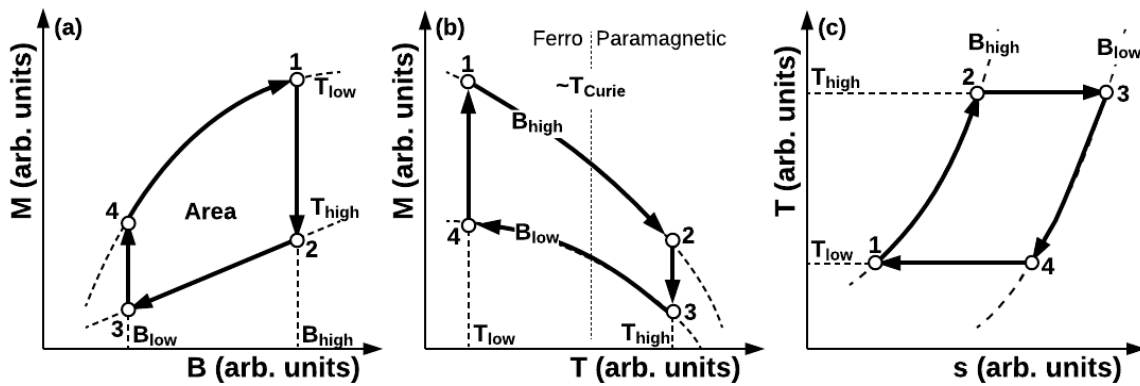
$$W = \oint TdS \qquad (2)$$

Figure 1. Thermomagnetic motor (Ericson) cycle: (a) M vs. B; (b) M vs. T; (c) T vs. s. Adapted from Christiaanse and Bruck (2013).
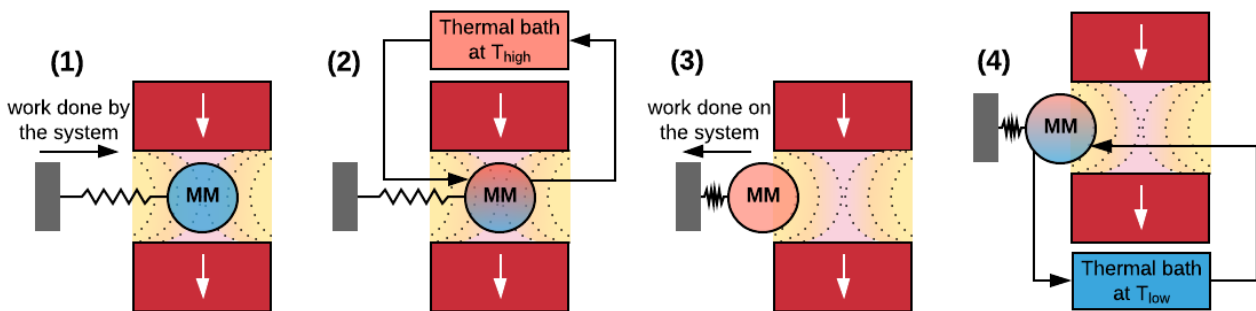

Figure 2. Schematic diagram of the Ericson cycle of a thermomagnetic motor. The red blocks with the white arrows represents the magnetic circuit; the color gradient in the magnetic field volume represents the iso-mangetic field lines; MM is the magnetic material; and the magnetic force is counterbalanced by a traction spring.

In the operation of a thermomagnetic motor two different streams (hot and cold) must be supplied to the magnetic material at different periods of the cycle: (1 to 2) and (3 to 4). Therefore, this kind of motor could be applied as heat recovery systems, using low temperature steam as hot stream.

The main components of a thermomagnetic motor are the permanent magnet magnetic circuit, the magnetic (or magnetocaloric) material, the pumping system and a converting system to convert the magnetic force into usable work

(work done by a shaft). The permanent magnet magnetic circuit is the most expensive and complex component of this system, and can be designed with different sizes and shapes such as: a hollow cylinder (HALBACH, 1980), C-shape Halbach circuit (BOHIGAS, 2000), Nested Halbach Cylinders (TREVIZOLI *et al*, 2015). Bjørk et al (2010) described different permanent magnet magnetic circuits and proposed a figure of merit to evaluate the "performance" of a magnet applied to a magnetic cooling system. An optimal magnetic circuit should use minimum amount of magnets, and generate a high magnetic field in a large volume (BJØRK *et al*, 2010).

This work presents the design and assembly procedure of a magnetic circuit which is under construction (in-house) at State University of Maringá. This magnet will be used as magnetic field source of a thermomagnetic motor apparatus. The designed magnet is a double-C type, composed by several NdFeB permanent magnets blocks arranged in Halbach array. This magnetic circuit, therefore, provides two high field regions, which will enable to study different configurations of the thermomagnetic motor. The magnet was designed via 2D and 3D simulations using COMSOL Multiphysics 5.3. The assembly procedure followed the work by Schäfer (2016). The final magnetic circuit is able to provide two high field regions with a maximum (averaged in volume) magnetic flux density intensity of 0.89 T.

2. METHODOLOGY

2.1 Magnet Assembly

The magnet design and assembly procedure follow the work by Schäfer (2016) at University of Victoria (Canada). The designed magnetic circuit is a double-C configuration, presented in Fig. 3, which is a association of permanent magnet (NdFeB) blocks in a Halbach array (red blocks in Fig. 3, where the white arrows indicate the remanence direction), and soft ferromagnetic material, such as Fe, FeCo or Steel alloys (dark gray in fig. 3). Halbach arrays enable to use less permanent magnet mass to produce a higher magnetic field, while the soft ferromagnetic material with a high relative permeability (μ_r) is used to guide the magnetic flux lines. The light gray regions in Fig. 3 are made of non-magnetic material only for structural purposes.
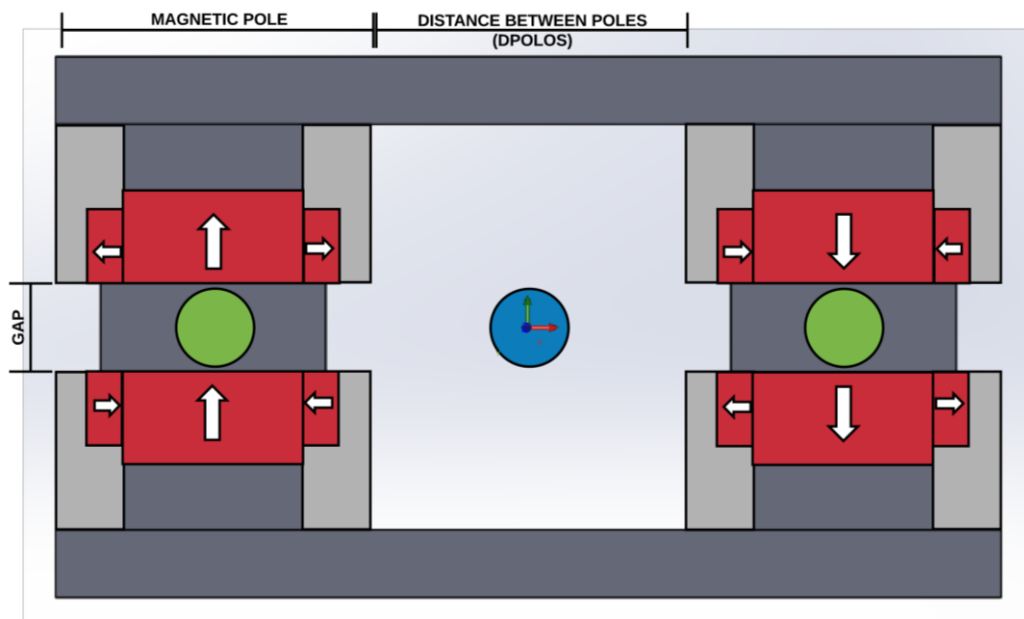

Figure 3. Double-C magnetic circuit design. The red blocks with the white arrows represents the magnetic circuit; the arrows indicate the remanence direction; the dark gray is the soft ferromagnetic material used to guide the magnetic flux lines; the light gray is a non-magnetic material used for structural purposes.

The present design used three different permanent magnet blocks with different purposes, as presented in details in Fig. 4. The first one is the *Main Magnet*, indicated by north and south pole in Fig. 4 and they are the biggest magnet blocks in Fig. 3. The second, is the *Side Concentrator*, indicated by side in Fig. 4 and are the smallest magnet blocks in Fig. 3. The last set of blocks, is the *Frontal Concentrator*, only presented in Fig. 4. The main magnets are positioned at the center of the magnetic pole and they are responsible to generate the high field volume. The concentrator magnets (side and frontal) are used to reduce the border effects, and then, guarantee a more homogeneous magnetic field volume with a higher field intensity.
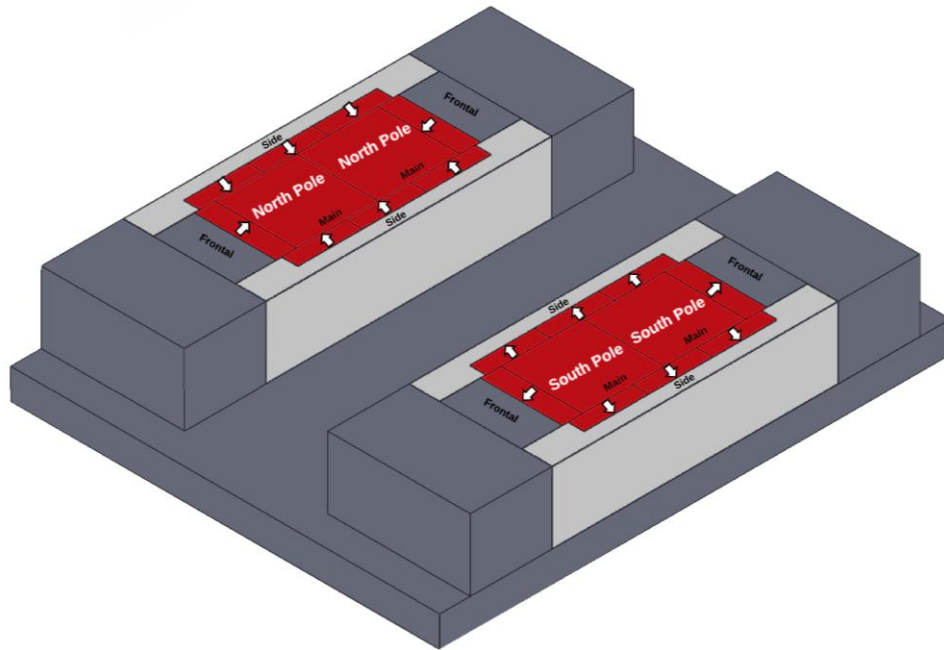
Figure 4. Details of the permanent magnet blocks distribution in the Halbach array. The red blocks with the white arrows represents the magnetic circuit; the arrows indicate the remanence direction; the dark gray is the soft ferromagnetic material used to guide the magnetic flux lines; the light gray is a non-magnetic material used for structural purposes.

2.2 Materials

As previously introduced, the designed magnetic circuit is under construction at State University of Maringá. This way, the materials used in the design - permanent magnets (NdFeB) and soft ferromagnetic materials - were selected according to their commercial availability, with a design target of maximum magnetic field around 1 T. As a result, the majority of the final dimensions of the magnetic circuit were adjusted according to the available sizes of the permanent magnet blocks. Table 1 summarizes the dimensions, type, remanence and maximum operating temperature of the selected NdFeB permanent magnets.

Table 1. Selected NdFeB permanent magnets and their properties.

Used as	Size (mm)	Grade	Remanence (T)	Max. Operating Temp (ºC)
Main	50,8x50,8x25,4	N50	1.41	70
Frontal	50,8x25,4x12,7	N50	1.41	70
Side	40x20x10	N42	1.32	70

After the selection of the permanent magnets, it was performed several 2D simulations to choose the best soft ferromagnetic material. It was initially analyzed 1006, 1008, 1010, 1018 and 1020 steel. The simulation results showed virtually no differences on the magnetic field intensity and distribution, however, only the 1020 steel was commercially available from local suppliers. It is important to mention that to both, 2D and 3D simulations, the model considered the dependency of the relative permeability of soft ferromagnetic materials (μ_r) on the magnet field, as illustrated in the Fig. 5 for 1020 steel.

2.3 2D simulation

Fig. 3 presents the 2D model used in the simulation. Again, the dark gray structure is 1020 steel the permanent magnets are in red. To perform the simulations, it is necessary to input the remanence intensity (in Table 1) and directions (illustrated in Figs. 3 and 4) of each permanent magnet blocks. The green circle represents magnetic material heat exchanger at the high field region (region of interest), and the blue circle is the low field region. Hence, the maximum magnetic field is the area-averaged field on the green circle, and the minimum averaged on the blue circle. Finally, to properly set the boundaries condition, the entire magnet was in the middle of an air square with 5080x5080mm size.
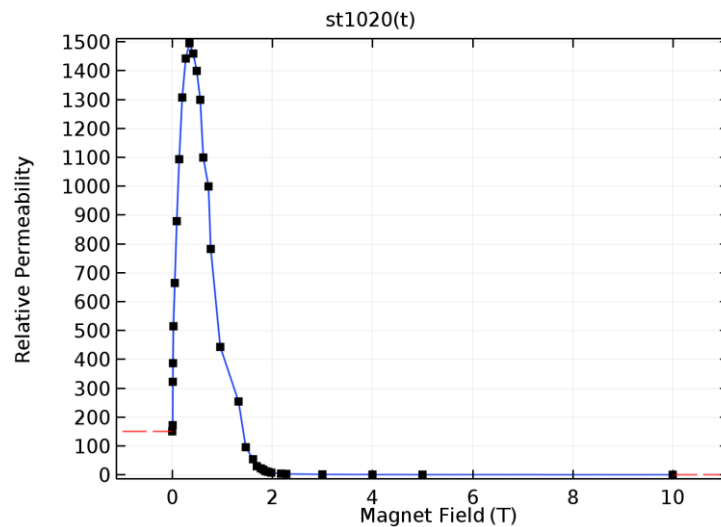
Figure 5. Dependency of the relative permeability on the magnet field for 1020 Steel.

The 2D simulations were performed using the software COMSOL Multiphysics (v. 5.3, AC/DC module, magnetic fields, no currents formulation). The magnetostatic formulation is modeled using the following equations:

$$H = -\nabla V_m \qquad (3)$$

$$\nabla \cdot (\mu_0 \mu_r H + B_r) = 0 \qquad (4)$$

$$B = \mu_0 \mu_r H + B_r \qquad (5)$$

where V_m is the magnet scalar potential, H is the magnetic field, μ is the magnetic permeability, B is the magnetic flux density, B_r is the remanence, and the subscribes r is relative, and 0 means in the vacuum. The 2-D simulations were carried out using a mesh of about 10114 elements with an average element quality of 0.894. A convergence tolerance of 10^{-5} was used.

As discussed in the previous section, 2D simulations were initially performed to select the soft ferromagnetic material. In the same direction, 2D simulations were also used to find the final magnet dimensions of the designed magnetic circuit, read: magnetic gap distance (GAP in Fig. 3) and distance between poles (D_{polos} in Fig. 3). It was performed a parametric study. For a fixed GAP of 25.4 mm, D_{polos} ranged from 44.45 mm to 181.6 mm in steps of 13.715 mm; while for a fixed D_{polos} of 88.9 mm, the GAP ranged from 12.7 to 38.1 mm in steps of 1.5875 mm. The target constraints for magnetic field are:

    (i)   area-averaged high magnetic flux density (green circle in Fig. 3) close to 1 T;
    (ii) area-averaged low magnetic flux density (blue circle in Fig. 3) as close as possible to 0 T.

2.4 3D simulation

The final dimensions resulted from 2D simulations were implemented in a 3D model in SolidWorks 2017 (Fig. 6 and 7), and then 3D simulations were also performed in COMSOL Multiphysics (v. 5.3, AC/DC module, magnetic fields, no currents formulation). The numerical results from the 3D simulation is a fundamental step towards a more realistic result, including border effects. In addition, enables the evaluation of the volume-averaged high magnetic field (which is the 3D equivalent of the green circle in Fig. 3), as well, the evaluation of the magnetic field profile along the axial direction (z-axis), which provides the necessary information to design the magnetic material heat exchanger.

The magnetostatic formulation solves the same equations for the 2D model (Eqs. 3-5). To properly set the boundaries condition, around the magnetic circuit it was defined an air block with 400x300x400mm size. The 3D simulations were carried out using a mesh of about 495919 tetrahedral elements with an average element quality of 0.70. A convergence tolerance of 10^{-5} was used.

For the 3D simulation, however, it was necessary to develop two versions in SolidWorks for the 3D model. The first one, is the complete design including all the drill holes and details. This version did not allow COMSOL to find a converged solution, possibly because of the extremely fine mesh around the drill holes. Hence, a second simplified version of the 3D model, presented in Fig. 6, was developed. In Fig. 6 it is presented three different cut plans: (1) Plan XY0, also presented in Fig. 7(a), enables to analyze the magnetic flux density distribution along the x-axis (center line);

(2) Plan ZY0; (3) Plan ZY88.9, also presented in Fig. 7(b), enables to analyze the magnetic flux density of the high field region along the z-axis (center line). The flux density distributions for both, Plan XY0 and Plan ZY88.9, are fundamental data to design the magnetic material heat exchanger and develop numerical models to simulate the thermomagnetic motor.
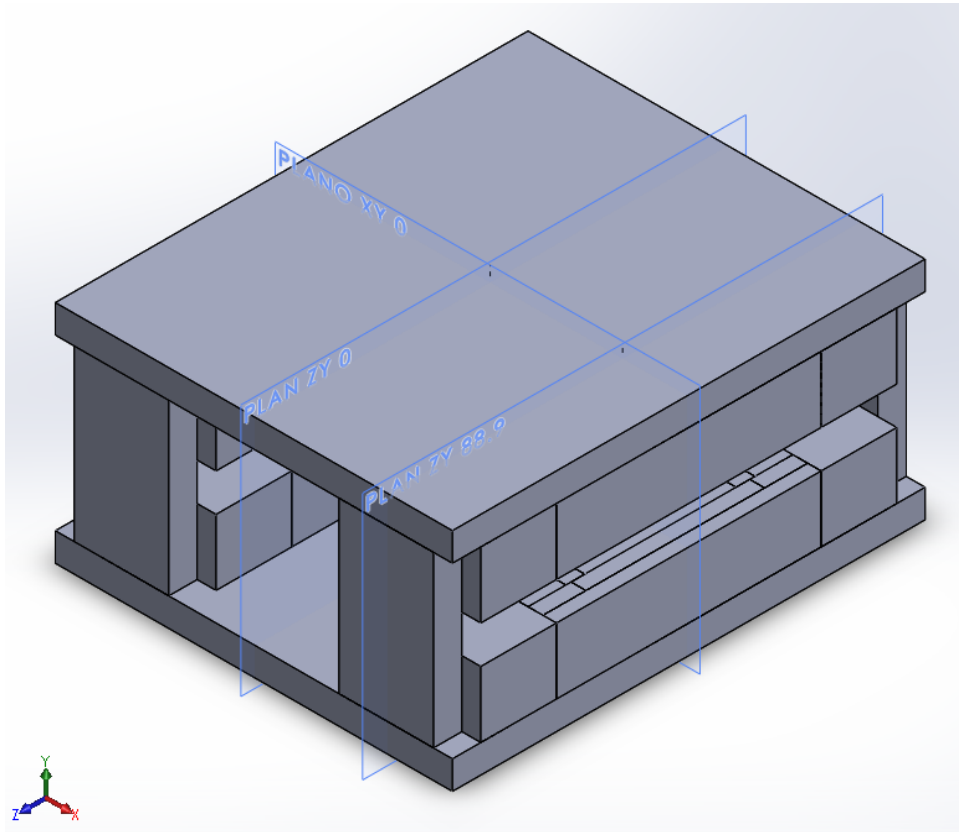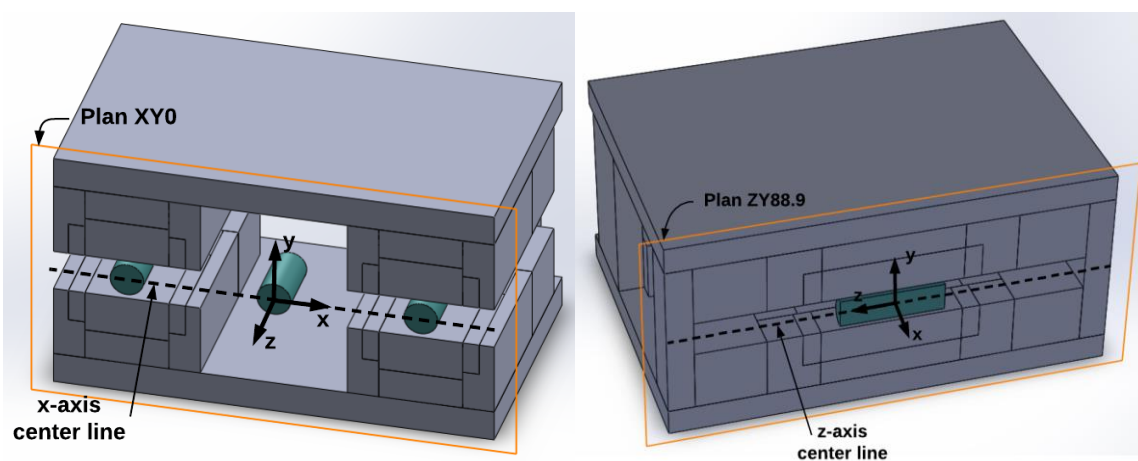

Figure 6. Simplified 3D SolidWorks model.

Figure 7. Details of the cut plans XY0 and ZY88.9, including the x-axis center line and z-axis center line.

3. PRELIMINARY RESULTS AND CONCLUSIONS

3.1 2D Simulation

Fig. 8 shows the magnetic flux density results for the parameterized distance between poles: Fig. 8(a) for the high field region (green circle in Fig. 3); Fig. 8(b) for the low field region (blue circle in Fig. 3). As ones can verify the dependence of the magnetic flux density on D_{polos} is small and, therefore, any D_{polos} satisfy the target constraints (i) and (ii). Thus, it was selected a dimension to $D_{polos} = 88.9$ mm, which provides some room to work inside the magnetic circuit (necessary to assembly of the thermomagnetic motor) and is not excessive large reducing the total weigh.
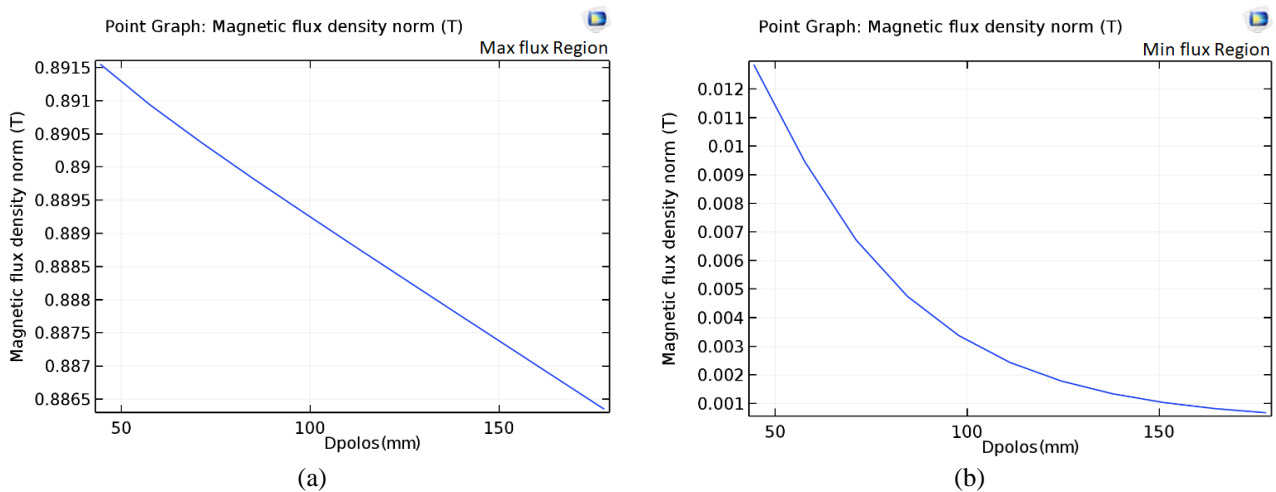

Figure 8. Results of the 2D simulation for the area-averaged magnetic flux density as a function of the parameterized distance between poles: (a) for the high field region; (b) for the low field region.

Fig. 9 shows the magnetic flux density results for the parameterized *GAP*. Again: Fig. 9(a) for the high field region (green circle in Fig. 3); Fig. 9(b) for the low field region (blue circle in Fig. 3). As expected, the highest magnetic field is observed at the lowest gaps, while the low magnetic field region presented small variations. In this case, any *GAP* ranging from 12.7 mm to 26 mm satisfy the target constraint (i) and (ii). This way, it was selected a gap of 25.4 mm (1 in) which provides high flux density at a large volume to assembly a larger amount of magnetic material to operate the thermomagnetic motor. A larger mass of magnetic material will provide higher force output signals (measurement), making possible better force or torque measurements with smaller uncertainties.

Therefore, the final dimensions for the *GAP* is 25.4 mm and D_{polos} is 88.9 mm. The 2D results for the area-averaged magnetic flux density of this combination is a high flux density of about 0.89T, and the low flux density is 0.004T.
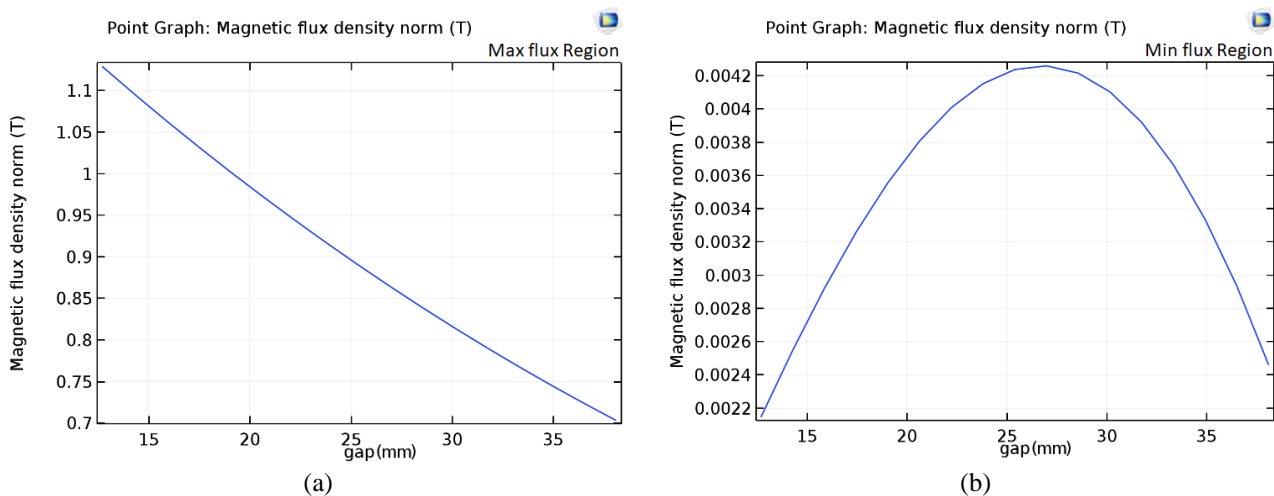

Figure 9. Results of the 2D simulation for the area-averaged magnetic flux density as a function of the parameterized gap: (a) for the high field region; (b) for the low field region.

3.2 3D Simulation

Fig. 10 shows the 3D simulation results of the cut plane XY0, which is the same plane of the 2D simulations. Fig. 10(a) is the magnetic flux density distribution along the plane XY0 (magnetic circuit and surroundings), where the red arrows indicate the direction of the flux density. Fig. 10(b) is the flux density profile along the x-axis (center line, see Fig. 7). The region of interest (circles at x ≈ ± 90 mm) have 0.89T average flux density, and the low field region is around 0 T (-50 < x < 50), as in the 2D simulations.

In addition, it is possible to verify the border effects. In Figs. 10(a), if one follows the color legend and the red arrows distribution in the high field region (air gap around the circle) it is visible the variation of the flux density from the center of the circle to the borders, resulting in the profile along the x-axis in Fig. 10(b). It is important to notice that if this magnetic circuit had not been designed with side concentrator magnets, the results for the field intensity and distribution would be lower than in the current design. Even though the border effects reduce the high magnetic field intensity, the field distribution along the x-axis it is an important feature for the proposed thermomagnetic motor. The magnetic material is placed (when paramagnetic) in a low field region slightly higher than 0T (see Figs. 1 and 2). Therefore, when the material is cooled down returning to the ferromagnetic phase, there is a residual low magnetic field to attract the magnetic material. The optimum position of the magnetic material when at the low field region is a key parameter to the design of the motor and will be evaluated after the final assembly of the motor apparatus.
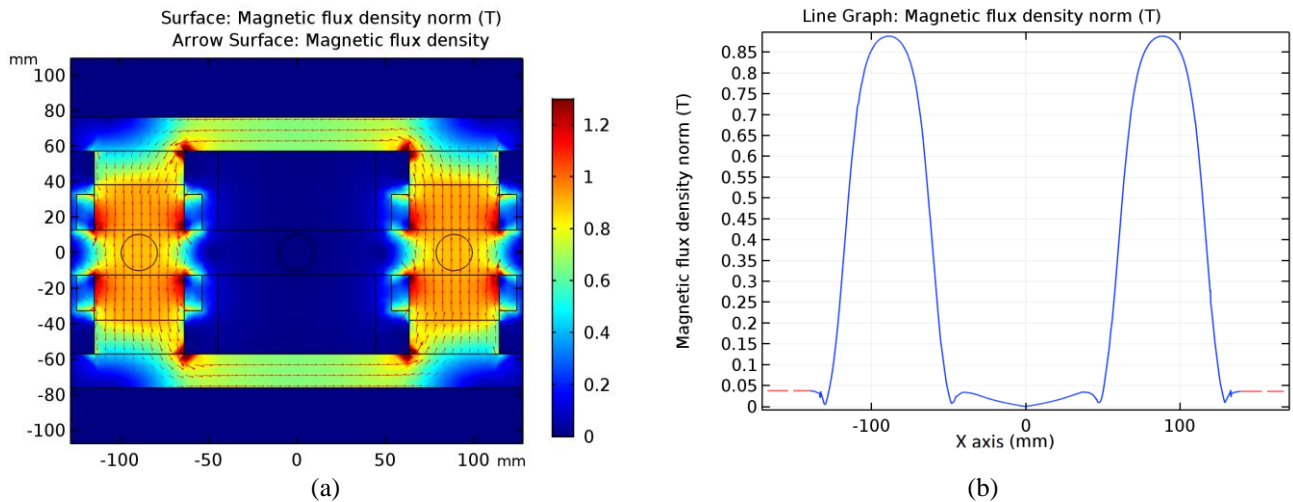

Figure 10. Magnetic flux density distribution: (a) along the Plan XY0; (b) along x-axis (center line, see Fig. 7). The red arrows indicate the direction of the flux density.

Fig. 11 shows the 3D simulation results of the cut plane XY88.9. Fig. 11(a) is the magnetic flux density distribution along the plane XY88.9 (magnetic circuit and surroundings). Again, the red arrows indicate the direction of the flux density. Fig. 10(b) is the average flux density profile along the axial direction (z-axis center line, Fig. 7).
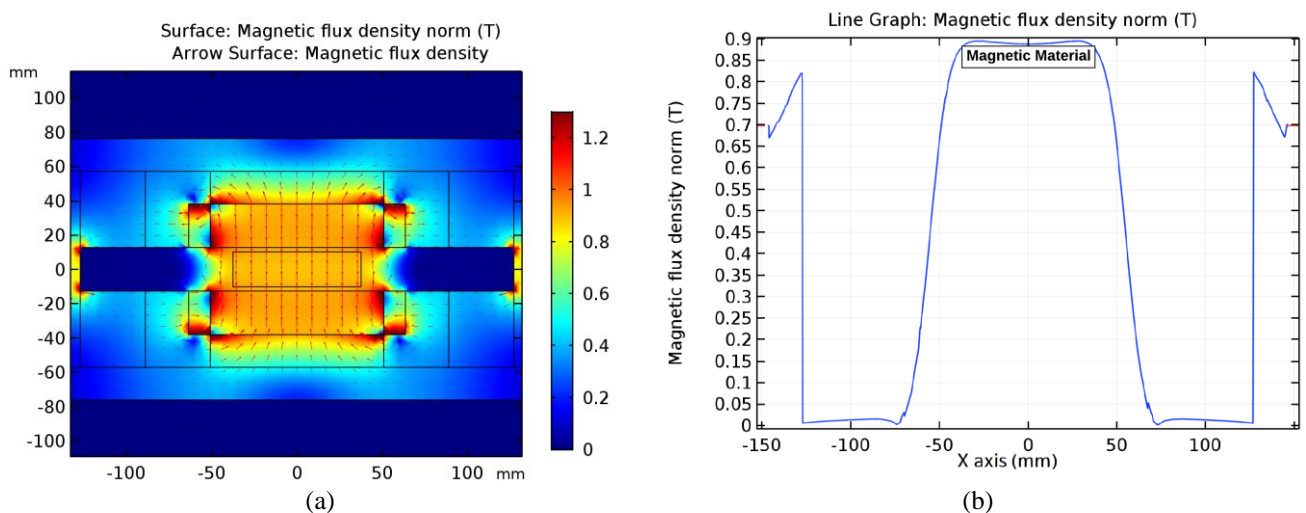

Figure 11. Magnetic flux density distribution: (a) along the Plan XY88.9; (b) along z-axis (center line, Fig. 7).

The axial distribution of the high field region presented a good homogeneity where the magnetic material is place (see the rectangular region in Fig. 11(a) and (b)). In this case, the border effects along the axial direction is the parameter that guide the magnetic material heat exchanger length. As ones can see in Fig. 11(b):

- Increasing the heat exchanger length it will increase the magnetic material volume and mass and, if the high magnetic field is nearly constant, increases the magnetic force (see Eq. 1).
- On the other hand, if the high field is not constant, the periphery parts of the heat exchanger length may not be subjected to a useful field strength. In addition, a longer heat exchanger will also have a larger viscous losses, which will reduce the motor efficiency.

Therefore, it must have an optimum length, which will be evaluated to design the magnetic heat exchanger. In this paper, it was placed in the high field region a volume emulating the magnetic material heat exchanger with 20-mm diameter and 75-mm length. The 3D results for the volume-averaged magnetic flux density on the heat exchanger volume is about 0.89 T to the high flux density, and 0.004 T to the low flux density region. As a conclusion, since there is virtually no differences between the 2D and 3D results for the averaged high and low magnetic flux densities, the proposed magnet design was successful, and the frontal and side concentrators magnets were well designed.

3.3 Double-C Magnetic Circuit Final Design

Fig. 12 shows the final design of the double-C magnetic circuit. In this SolidWorks model it is possible to verify the drill holes and another structural details. One interesting feature included in the magnetic circuit design is the possibility to change the *GAP* using two large screws. While the bottom plate magnets are fixed, the top plate magnets can be moved up and down, and consequently, changing the magnetic flux intensity (see Fig. 9(a)). The possibility to change the magnetic field enable to perform advanced studies towards the optimization of field intensity versus magnetic material volume/mass, as well, the designed magnetic circuit can be used to perform other experimental research under development at State University of Maringá.
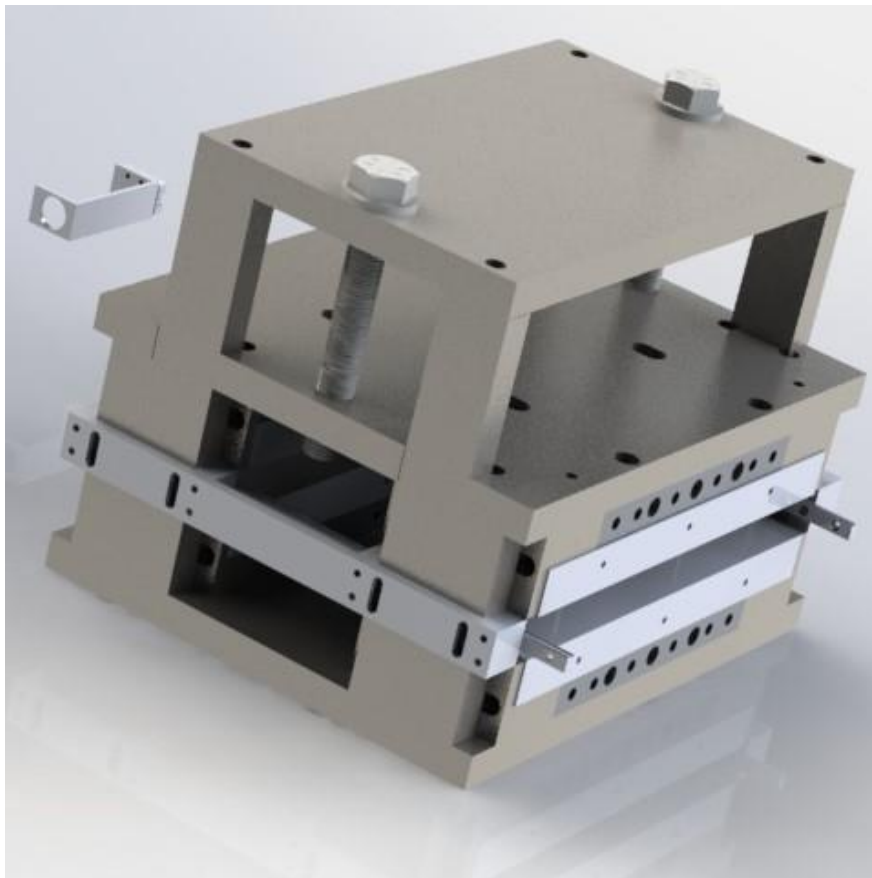

Figure 12. Final design of the double-C magnetic circuit.

4. CONCLUSION/ADDICTIONS TO THE FINAL PAPER

In this work we presented a complete description of the design and simulation results of a double-C magnetic circuit. The designed magnet is currently under construction at State University of Maringá. All the selected materials were purchased from local suppliers. It was found from the 3D simulations that a *GAP* of 25.4 could provide an

volume-averaged high magnetic flux density of 0.89 T, which is close to the target value of 1 T. At the same time, the designed *GAP* enables the assembly of a good volume of magnetic material which would guarantee reasonable ranges of force or torque to be measured in the motor apparatus.

To the final paper, we are expecting to present the assembled magnet. If successful, the designed double-C magnetic circuit will enable to perform experimental studies of different magnetic material heat exchanger arrangements, which will be a novel study when compared with thermomagnetic motors found in the open literature.

5. ACKNOWLEDGEMENTS

6. REFERENCES

Alves, C., Colman, F., Foleiss, G., Szpak, W., Vieira, G., Bento, A., 2014, "Simulation of Solar Curie Wheel using NiFe alloy and Gd". International Journal of Refrigeration, 37, 215-222.

Barclay, J. A., Steyert, W. A., 1982. "Active magnetic regenerator". US Patent 4332135.

Bjørk, R., Bahl, C.R.H., Smith A., Pryds N., 2010, "Review and Comparison of Magnet Designs for Magnetic Refrigerator". International Journal of Refrigeration, 33, 437-448

Bohigas, X., Molins, E., Roig, A., Tejada, J. Zhang, X., 2000, "Room Temperature magnetic refrigerator using permanent magnets." IEE Transactions on Magnetics, 36, 538-544.

Christiaanse, T., Brück E., 2013. "Proof of concept Static Thermomagnetic Generator Experimental Device", Metallurgical and Materials Transactions E, 1, 36-40.

Edison, T.A. 1888, "Pyromagnetic motor". US Patent 380100.

Gschneidner, K., Pecharsky, V., (2008), "Thirty years of near room temperature magnetic cooling: Where we are today and future prospects", International Journal of Refrigeration, 31(6), 945-961.

Gutfleisch, O., Gottschall, T., Fries, M., Benke, D., Radulov, I., Skokov, K.P., Wende, H., Gruner, M., Acet, M., Entel, P., Farle, M., 2016. "Mastering hystereis in magnetocaloric materials". Philos Trans A Math Phys Eng Sci, 13, 374.

Halbach, K., 1980, "Design of permanent multipole magnets with oriented rare earth cobalt material". Nuclear Instruments and Methods, 169(1), 1-10.

Karle, A., 2001, "The thermomagnetic Curie-motor for the conversion of heat into mechanical energy". Int. J. Therm. Sci., 40(9), 834-842.

Pecharsky, V.K., Gschneidner Jr., K.A., Pecharsky, A.O., Tishin, A. M., 2001. "Thermodynamics of the magnetocaloric effect". Phys. Rev. B, 64, 144406.

Schäfer B., 2016. *Development of a Magnetocaloric test apparatus.* Master Thesis, Faculty of Mechanical Engineering, Munich.

Smith, A., Bahl, C.R.H., Bjork, R., Engelbrecht, K., Nielsen, K.K., Pryds, N., 2012. "Materials challenges for high performance magnetocaloric refrigeration devices". Adv. Energy Mat., 2(11).

Tesla, N., 1889. "Termo-magnetic motor". US Patent 396121.

Trevizoli, P., Lozano, J., Peixer, G., Barbosa, J., 2015, "Design of Nested Halbach cylinder arrays for magnetic refrigeration applications", Journal of Magnetism and Magnetic Materials, 395, 109-122.

Trevizoli, P. V., Christiaanse, T. V., Govindappa, P., Niknia, I., Teyber, R., Barbosa Jr., J. R., Rowe, A., 2016. "Magnetic heat pumps: An overview of design principles and challenges". Science and Technology for the Built Environment, 22, 507–519.

7. RESPONSIBILITY NOTICE

The authors are the only responsible for the printed material included in this paper.